Insights into Accelerated Degradation of Perovskite Solar Cells under Continuous Illumination Driven by Thermal Stress and Interfacial Junction

Dhruba B. Khadka†*, Yasuhiro Shirai†, Masatoshi Yanagida† and Kenjiro Miyano†

†Photovoltaic Materials Group, Center for GREEN Research on Energy and Environmental Materials, National Institute for Materials Science (NIMS), 1-1 Namiki, Tsukuba, Ibaraki 305-0044, Japan.

ABSTRACT

The operational stability of encapsulated halide perovskite solar cells (HaPSCs) is imperative for their commercialization. Despite improvements in device stability, we lack insights into the irreversible degradation of devices under prolonged illumination and heat stress. Here, we investigated the operational stability of devices (~1 cm^2) made with poly(triaryl amine) (PTAA; power conversion efficiency PCE ≈ 19.32%) and sputtered NiO_x (PCE≈15.60%) as a hole-transport layer (HTL) under light (for >1000 h) at 20, 60, and 85 °C to unravel the degradation mechanisms. Degradation of the PTAA device was accelerated by interface deterioration and bulk decomposition initiated by the formation of voids and PbI_2 via iodine migration from defective regions at the columnar grain boundaries with the release of I_2 gas. The NiO_x device, with its immunity to iodine and its moisture-resistive properties, had significantly improved stability with suppression of the HaP bulk degradation by alleviation of internal defect dynamics. Our results corroborate that the formation of voids and PbI_2 crystallites at columnar inter-grains or at the HTL (ETL) /HaP interface with the release of I_2 gas is the primary cause of device degradation. Capacitance–voltage analysis showed that the PTAA device develops a much wider defective interface layer than the NiO_x device, driven mainly by the chemical reaction of iodine with the interfacial layer. Thus, our results reveal that although the cracking of columnar inter-grains and defective spots in the perovskite bulk is the main origin of device degradation, the nature of the carrier transport layer also partly contributes to catalysing bulk and interface degradation. Thus, the passivation of columnar inter-grain defects in the HaP bulk and lamination of the interface with a chemically inert to iodine and a moisture-resistive carrier-selective layer is crucial to the operational stability of HaPSCs.

Keywords: Perovskite degradation, device stability, iodine migration, nickel oxide, interfacial deterioration, columnar inter-grains, electrode corrosion, capacitance spectroscopy,

1. Introduction

The startling progress in the power conversion efficiency (PCE) of halide perovskite solar cells (HaPSCs) is now getting close to the theoretical limit for single-junction solar cells. [1–3] However, the commercialization of HaPSCs is limited by problems of long-term stability. [4–6] Despite the high device efficiency, real-world operation accelerates PCE loss. The degradation of HaPSCs is triggered by many causes, such as irradiation, heat, moisture, oxygen, electric bias, and strain.[7–10] These stimuli degrade the HaP film by accelerating bulk layer decomposition, ion migration, and dissociation of constituents. Diffusion through the electrode and deterioration of the carrier transport layer (CTL) are also notorious.[11–13]

Although encapsulation can suppress the degradation of HaPSCs by external causes, [14,15] HaP bulk degradation eventually starts to impede operational stability. [16] Multiple studies have been devoted to understanding the intrinsic degradation of HaPSCs. [17–19] In particular, under heat–light soaking (HLS) conditions, iodine vapour released from defective regions induces degradation that propagates across the active area, forming voids with PbI_2-rich regions and decreasing the photocurrent. [18,19] Degradation is instigated mainly from domains richer in defect densities such as grain boundaries [20] and the interface with CTLs. [21] Noting these factors, several reports have attempted to improve the intrinsic stability by engineering the HaP film with a mixed composition, [22] large organic cations as a hydrophobic interface, [23] molecular additives, [24] and tailoring of the CTLs/interfaces. [25,26]

Recent operational stability studies have focused on the degradation mechanisms. [16,27] Besides the intrinsic stability of the HaP layer, the CTL and its interface also have a crucial role in device stability. Grätzel and co-workers reported excellent operational stability using CuSCN and a reduced graphene oxide spacer layer that prevents electrode corrosion. [28] Yang et al. reported improved stability by passivating the HaP surface with lead sulphate as a protective layer. [29] Cui and co-workers improved stability by passivating the surface and grain boundaries, forming a 1D/3D perovskite heterojunction with the introduction of propargylammonium to the 3D HaP film. [30] Troshin and co-workers suggested that the degradation of HaP can be suppressed with CTLs that are chemically robust to the chemical constituents of the absorber layer. [31] Though most operational stability data are acquired at room temperature, stability at higher temperatures is more pertinent to real-world devices that can reach 80 °C. [6] Schloemer et al. [11] documented comprehensive insights into the interface effect for operational stability of HaPSCs. They dramatically improved high-temperature operational stability by replacing MoO_x with VO_x. A rapid loss of short-circuit density (J_{sc}) of the device caused by buckling of the hole-

transport layer (HTL)/MoO_x interface can be decelerated by interface modification with the VO_x interlayer. Even though the degradation mechanism is stimulated at elevated temperatures through an increase in chemical kinetics that leads to interfacial deterioration as well as delamination, the mechanisms that cause operational instability of HaPSCs with different interface layers remain largely elusive. There are still open questions of how the degradation propagates under HLS stress and how the CTL catalyses the device degradation. Therefore, it is imperative to get insight into accelerating stress testing to provide hints for interface engineering and device stability.

Here, we systematically investigated the operational stability of perovskite solar cells at different temperatures under constant illumination in an ambient atmosphere. We evaluated the operational stability of HaPSCs with poly(triaryl amine) (PTAA) or NiO_x as the HTL to understand the degradation mechanisms. Scanning transmission electron microscopy (STEM) and energy-dispersive X-ray (EDX) spectroscopy results revealed that the degradation of PTAA device is accelerated by interface deterioration followed by bulk decomposition initiated by the formation of voids and PbI_2 crystallites at columnar inter-grains or the HTL/HaP interface with the release of I_2 gas. In contrast, the interface of NiO_x devices remained comparatively stable by blocking iodine migration and hence decelerating bulk decomposition. X-ray photoelectron spectroscopy (XPS) analysis reveals that the PTAA layer easily deteriorates as it interacts with iodine or its derivatives under ageing. A thin layer of NiI_2 that forms at the surface of NiO_x as it interacts with iodine could change the interface band offset and hence increase the open-circuit voltage (V_{oc}) of the device. We also investigated the optoelectronic deterioration of aged devices by analysing capacitance spectra. This work illustrates the mechanism of device degradation and the nature of the HTL under HLS conditions that is crucial to resolving operational stability problems.

2. Results and discussion

We fabricated inverted-based HaPSCs with HTLs made of PTAA or NiO_x (Fig. 1a). Figure 1b displays *J–V* curves of devices of 1 cm^2 (Fig. S1), with their figures of merit inset. The PTAA device had a device efficiency of 19.32%; the sputtered NiO_x device had an efficiency of 15.60%. These results are in the range of best reports for large-area devices. [32] Our previous study analysed the effect of HaPSCs with an HTL/PTAA or HTL/NiO_x interface.[33] It is found that the perovskite film grown on PTAA/ITO has larger grain, fewer grain boundaries, and lower defect states compared to the perovskite film prepared on NiO_x/ITO which led to better device performance. Moreover, the properties of the HTL not only impact the crystal growth and optoelectronic properties of the perovskite layer but also influence the device operational stability. The HaPSCs with PTAA and NiO_x have different degradation rates because the PTAA and NiO_x have different interface chemistries and interactions

with external stimuli.[34,35] In this work, we focus to get insights into the degradation phenomena of these devices under thermal and light stress.

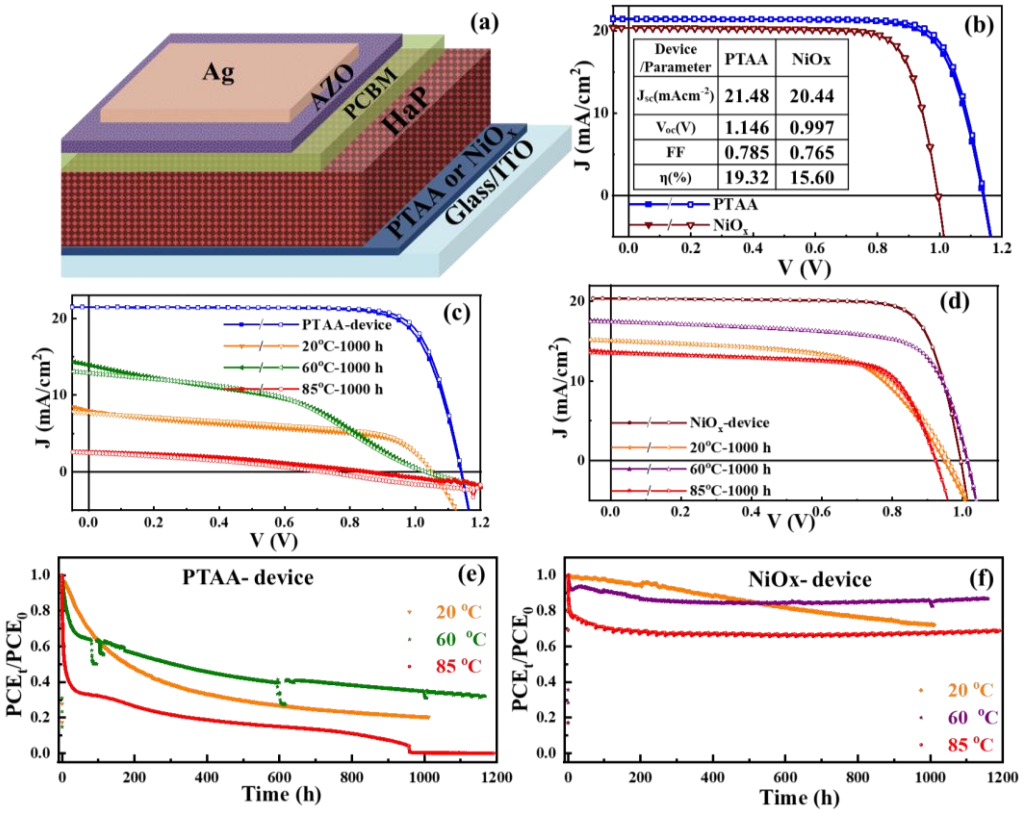

Figure 1. (a) Device configuration of HaPSCs: ITO/PTAA or NiO_x/HaP/PCBM/AZO/Ag. (b) current density–voltage (*J–V*) curves of the best HaPSCs (■▼ forward / □ ▽ reverse scan direction). (c, d) *J–V* curves of aged devices with (c) PTAA and (d) NiO_x under different ageing conditions. (e, f) Long-term operational stability of the respective devices at different temperatures under maximum power point condition (1 sun).

To understand the mechanism behind the degradation, we monitored operational stability at 20, 60, and 85 °C under continuous illumination for >1000 h (Figs S2a-c, Table S1). Photographs of degraded devices are shown in the Supporting Information (Fig. S3, S4). One can see a stark difference in the appearance of the illuminated part of the PTAA device: the electrode seems to be damaged while the surroundings are faintly yellowish (Figs S2d, e). We attribute the ageing to the diffusion of Ag/iodine and the formation of PbI_2. Those features are starkly shown in the PTAA device compared with the NiO_x device.

The current density–voltage (*J–V*) curves in each condition were automatically plotted after set intervals during illumination (Figs S5; 1c, d). At maximum power point (MPPT), the aged NiO_x devices retained 72.84% of PCE_0 at 20 °C, 86.75% at 60 °C, and 68.72% at 85 °C, whereas the PTAA device dropped to 22.53%, 35.92%, 2.02%, respectively, of PCE_0 (Table S2). The degradation trends

of device parameters under different conditions are shown in Fig. S6. The NiO_x devices had superior stability. The degradation trend is governed by the J_{sc} trend, as in other reports.[11,18,34] The PTAA device lost J_{sc} much faster with ageing, which led to faster degradation, than the NiO_x device. The rate of change of J_{sc} of both devices is faster at 85 and 20 °C than at 60 °C which leads to an initial steep drop in PCE. A similar trend was observed in the earlier reports.[12,36] This abrupt initial loss in PCE could be due to the collective effect of the structural deformation of CTL, structural defect of the HaP layer, and CTL/HaP interface of either side under higher thermal stress under the light.[12,37] Although a faster degradation rate is expected with an increase in temperature, the degradation rate of the device at 20 °C is higher than at 60 °C. It has been documented that the structural transformation of $MAPbI_3$ occurs as a function of temperature, thermal stress time, or halide additive.[37–39] Besides that, the co-existence of the tetragonal and cubic phases was also observed at room temperature.[40] These reports suggest that more structural defects are formed at a lower temperature (T~20 °C) while the structural defects are mitigated at 60 °C to some extent. Since structural defects are more sensitive to external stimuli, this could be one of the major reasons for better stability at 60 °C. Moreover, a faster degradation might be partly influenced by the moisture in the ambient air because the relative humidity in the enclosed testing system is higher at a lower temperature (T~20 °C). Indeed, the edges of the sealed device are still vulnerable to ingress of moisture from moisture-rich enclosed ambient.[7] Since PTAA is less moisture resistive compared to NiO_x, the device performance of PTAA is more prone at lower temperatures. It is further accelerated under additional light stress. We found that the PTAA device aged at 85 °C is dead, while the NiO_x device is still working, with lower J_{sc}. This must be dominated by characteristics differences in the interface as well as bulk deterioration of HaPSCs with PTAA and NiO_x. Similarly, the V_{oc} of the NiO_x device (Fig. S5) shows a slightly increasing trend with ageing, while that for the PTAA device decreases. We also note a slight loss in the fill factor of both devices (Fig. S6). This could be partly associated with a gradual increase of the series resistance (R_s) of the devices (Fig. S7). We noticed that the R_s of device with PTAA significantly increased with aging that could be stemmed from degradation of both PTAA and HaP bulk layer. As the PTAA film absorbs a high-energy photon (Fig. S8) under illumination and thermal stress, there is stretching of hydrocarbon ring and polymer chain in PTAA molecules that leads to partial decomposition of the cyclic structure under a longer aging stress environment.[34] As the deteriorated PTAA interacts with highly mobile iodine, it triggers the PTAA/HaP interface and bulk deterioration and hence increases the degradation rate. We will discuss the post-mortem analysis of the aged devices to unravel the degradation mechanism.

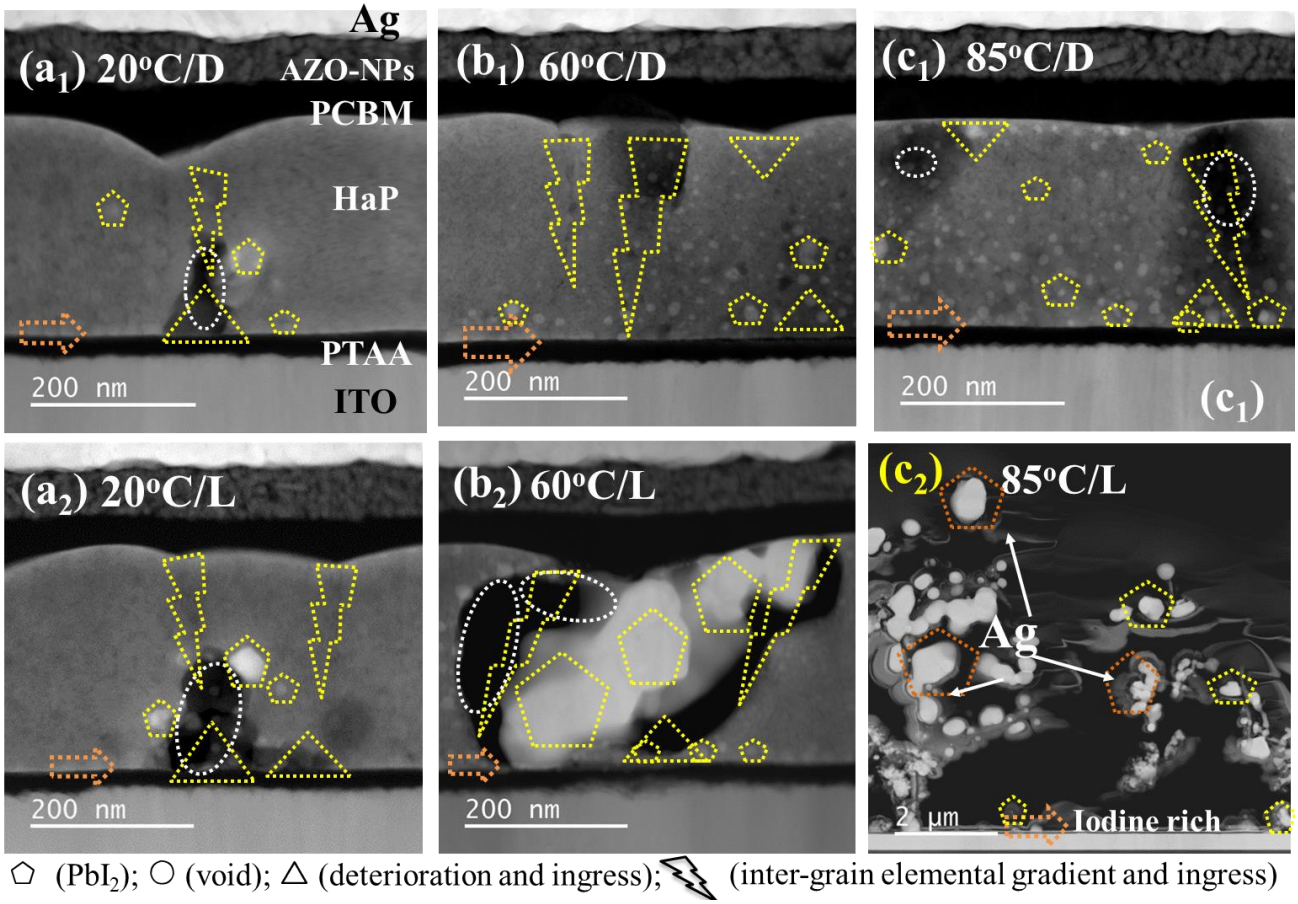

Figure 2. Dark-field STEM cross-sectional images of PTAA-device under stress ageing: a_1, b_1, c_1, 20, 60, and 85 °C in dark; a_2, b_2, c_2, under continuous illumination for 1000 h. Symbols: ➡ indicates PTAA/HaP interface.

To gain an insight into aged devices, we carefully removed the encapsulating cover glass without damaging the device layers. We delved into the bulk and interfacial deterioration and elemental diffusion in aged devices using TEM analysis (Figs. S9-18). A series of dark-field STEM images depict cross-sectional images of aged PTAA (Figs 2, S9) and NiO_x (Figs 3, S10) devices under different conditions. The STEM images and elemental mapping of fresh devices are given in supporting information (Figs. S17 and S18). There are distinct degradation features in the bulk and interface under dark and light at different temperatures. EDX analysis (elemental mapping; Figs S11, S12) and the line profile (Figs. S13) of each PTAA device are given in Supporting Information. Cross-sectional images of PTAA devices reveal more severe damage under photo-thermal ageing than in the dark, following a different route. The PTAA device aged in the dark shows bulk degradation with the formation of small crystallites of PbI_2 at the PTAA or PCBM/HaP interfaces, which increases in number with temperature. The PTAA device aged under light degraded faster by growing voids at the interface along with the formation of PbI_2 and interfacial deterioration. A narrow elemental line profile at the inter-grains (Fig. S13) suggests that iodine migrates through the inter-grains, triggering

decomposition and rupturing of the bulk layer. We also note iodine diffusion into the PTAA layer (Fig. S12-c_4). The $MAPbI_3$ bulk decomposes mainly to I_2, CH_3I, and CH_3NH_2 gaseous products, along with a small proportion of NH_3 and HI. [18] It eventually forms voids in the HaP bulk or at the interface with ingress of degradation gases such as I_2 vapour under prolonged illumination. Interestingly, although the void extended throughout the bulk cross-section, no Ag diffusion was observed in the other aged devices except that aged at 85 °C/light (Fig. S12-c_7). HaP bulk decomposition continues with the formation of PbI_2 and I_2 vapour, which exerts pressure within the device. [18] Since the PTAA layer absorbs the high energy photon (Fig.S8), with prolonged illumination, UV light could induce a more adverse effect on PTAA. [34] The PTAA layer also becomes less conductive with iodine diffusion and partial decomposition of the cyclic structure under aging stress environment. This results in an increase in series resistance by lowering the fill factor and J_{sc} of the device. In addition, the degradation gases corrode the interface, leading to Ag diffusion in the bulk HaP, and eventually rupture the top electrode through the corroded interfacial layer to release the high vapour pressure. Buecheler and co-workers [18] reported a similar observation of degraded HaPSCs. However, the iodine diffusion through PCBM or AZO layer and corroding the Ag electrode cannot be neglected in the solar cells with halogen-containing absorber layer.[13,41,42]

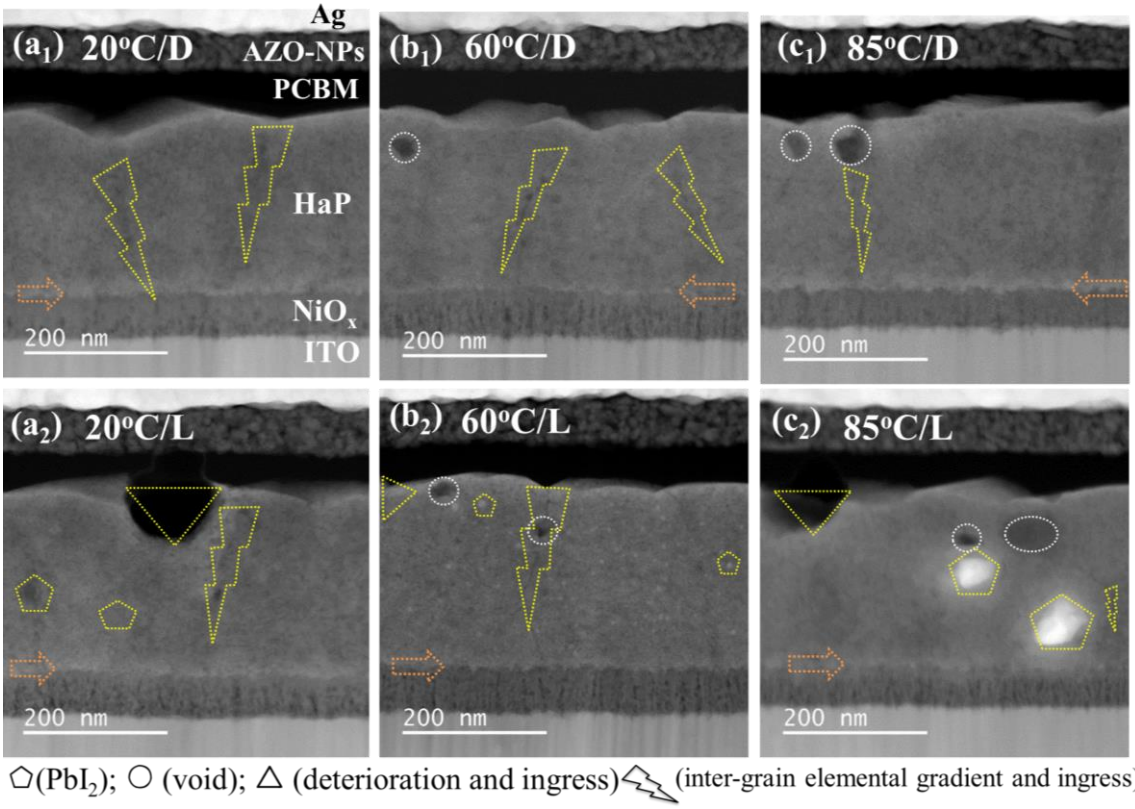

Figure 3. Dark-field STEM cross-sectional images of NiO_x-device under stress ageing: a_1, b_1, c_1, 20, 60, and 85 °C in dark; a_2, b_2, c_2, under continuous illumination for 1000 h. ➡ denotes NiO_x/HaP interface.

In the NiO_x device (Figs. 3, S17), one can see a much smaller effect of HLS in the HaPSC bulk than in the PTAA device. The elemental mapping and EDX line profile (Figs S13–S15,S18) show the only stark difference in the decomposition of the HaP bulk into PbI_2 at 85 °C/light. Unlike in the PTAA device, the NiO_x/HaP interface seems to be more robust. Although there are no obvious voids in the absorber layer, the initial stage of void formation seems to be triggered by the ingress of an inter-grain elemental gradient as a consequence of heat and light stress. Importantly, we also note a slight fluctuation of iodine at the NiO_x (PCBM)/HaP interface of the illuminated device (Fig. S16a_2-c_2), which could be the source of NiI_2 reported previously. [35] We saw no Ag diffusion except in the PTAA device at 85 °C/light (transparent conducting oxide layer ruptured, Fig. S9c_2) because of the robust aluminium doped zinc oxide (AZO) -layer beneath the Ag electrode that prevents Ag diffusion to the bulk. [43] Thus, the results corroborate that the NiO_x device has more robust interface that retards the defect chemistry at inter-columnar grains and the interface, and it protects against the decomposition of perovskite by preventing iodine migration or the formation of I_2 gas.

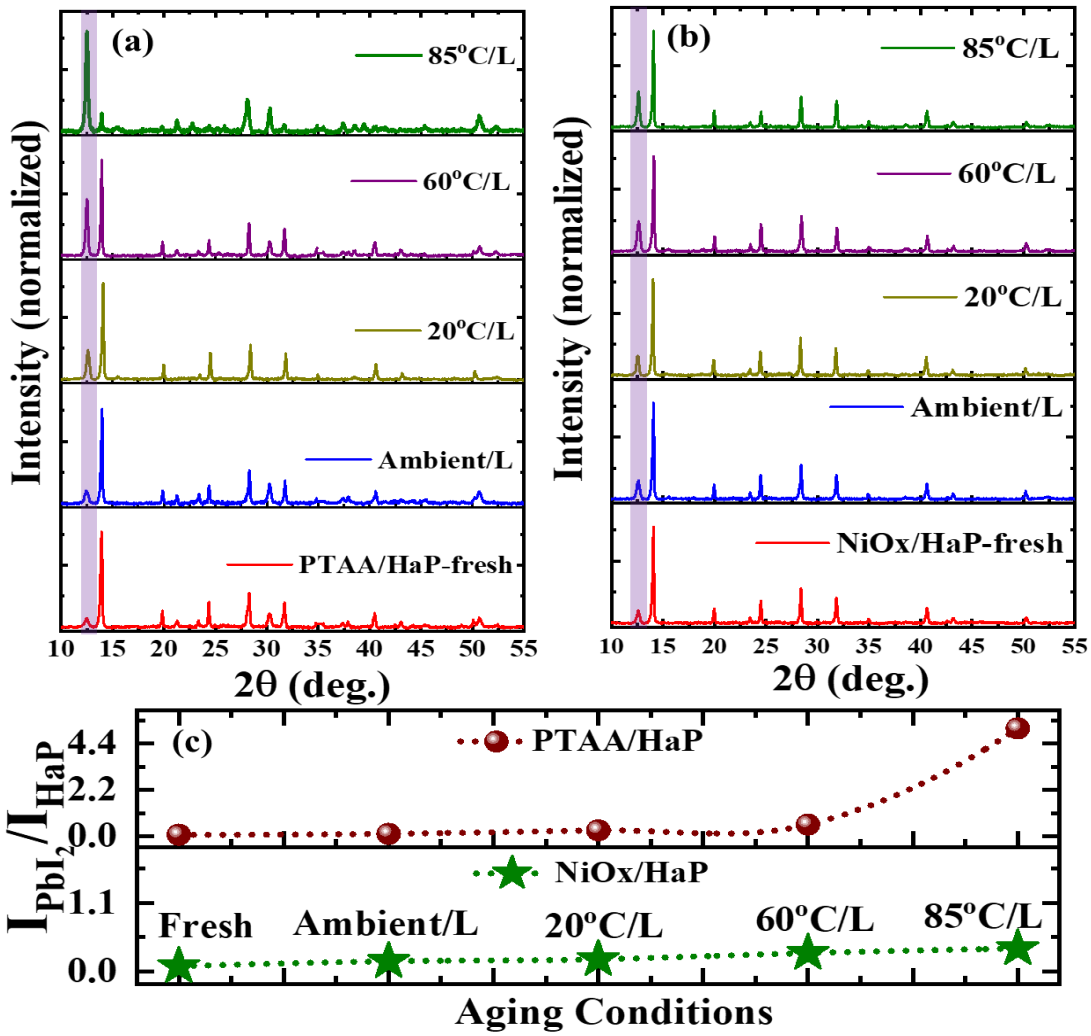

Figure 4. (a, b) XRD patterns of HTL/HaP films: (a) PTAA/HaP; (b) NiO_x/HaP; shading indicates PbI_2 peaks. (c) Ratios of evolution of PbI_2 to characteristics dominant XRD peak of HaP under different heat and light conditions for 200 h.

To gain further insights into the degradation, we measured the X-ray diffraction (XRD) patterns of HTL/HaP films treated under different heat and light conditions (Fig. S19). The patterns (Fig. 4a, b) give the characteristic diffraction peaks of PTAA/HaP and NiO_x/HaP. Figure 4c presents the ratios of intensity of PbI_2 and the HaP phase peak in the respective films under different ageing conditions. In the PTAA/HaP film, the (001) peak of PbI_2 (shaded region) gradually intensified relative to the (110) peak of the HaP phase with an increase in temperature, predominant at 85 °C/light. On the other hand, the peak is much less in the NiO_x/HaP film under the same ageing conditions. These results concur with STEM-EDX observations of PbI_2 in degraded devices: I_2 vapour-rich ambient conditions accelerate HaP degradation, forming the PbI_2 phase.[19] Thus, the growth of PbI_2 peaks in the PTAA device must be correlated with the release of I_2 in the bulk layer under HLS conditions. A lower PbI_2 peak in NiO_x/HaP must be a consequence of passivation of the I_2 gas formation mechanism by deactivating the photoactive iodine-related defect dynamics in the bulk.[44]

The degradation of HaP in the encapsulated device is triggered mainly by heat and light, which leads to decomposition into PbI_2 (s), CH_3NH_2 (g), HI (g), and I_2 (g).[52–54] The trapped by-product gases interact primarily with the HTL and the electron transport layer (ETL). Therefore, to provide mechanistic insight into the effect of the decomposed gases on the HTL and ETL, we set up an experiment for the interaction of PTAA, NiO_x, and phenyl-C_{61}-butyric acid methyl ester (PCBM) with methylammonium iodide (MAI) and I_2 vapour ambient under heat and light (Fig. S20). The surface chemistry was investigated by XPS analysis. XPS spectra (Figs. S21, S23, S24) for NiO_x (Ni2p, O1s, I3d-core),[48,49] PTAA (C1s, O1s, I3d-core),[50] and PCBM (C1s, O1s, I3d-core),[51] fresh and treated under different conditions, were fitted in consideration of the standard XPS reference [52]. The NiO_x film was significantly influenced by various treatments. An intensified Ni^{2+} peak in the Ni2p-core [48] and a diminished NiO peak in the O1s-core indicate the formation of NiI_2 under I_2 vapour. This result is supported by the change of the Ni^{3+}/Ni^{2+} ratio in NiO_x films (Fig. S22) under different treatments. The surface compositions extracted from the XPS spectra (Table S3) and evaluation of the I3d-core further confirm the formation of NiI_2 under I_2-rich vapour ambient and heat stress, but MAI vapour ambient is not as adverse. I3d-core spectra of the NiO_x film of an aged working device whose surface was exposed by peeling off the HaP and other layers suggest the formation of a thin NiI_2 layer at the NiO_x/HaP interface. This implicates the interaction of the NiO_x with migrated iodine or I_2 vapour. Other reports also have discussed the possibility of the formation of NiI_2 in aged devices that could be

detrimental to device performance. [53,54] Similarly, the C1s, O1s, and I3d core spectra (Fig. S23) reveal additional features in the PTAA film treated under different conditions. The I3d-core spectra under I_2 and MAI treatment and the surface composition (Table S4) show intercalation of iodine in PTAA that deteriorates it. The characteristics of the peeled-off PTAA imply that chemical reactions with the gases denature the PTAA and PTAA/HaP interface. The spectra of PCBM films also give distinct features under different conditions (Fig. S24). The I3d-spectra and composition (Table S5) substantiate that the decomposed gases adulterate the PCBM layer and the PCBM/HaP interface. The XPS results suggest that the CTL is vulnerable to attack by the gases (I_2, MA, HI) and hence degrades faster. Therefore, it is crucial to stabilize the HaP bulk to prevent the formation of degradation by-product gases as a consequence of the decomposition of HaP films that could denature the CTLs.

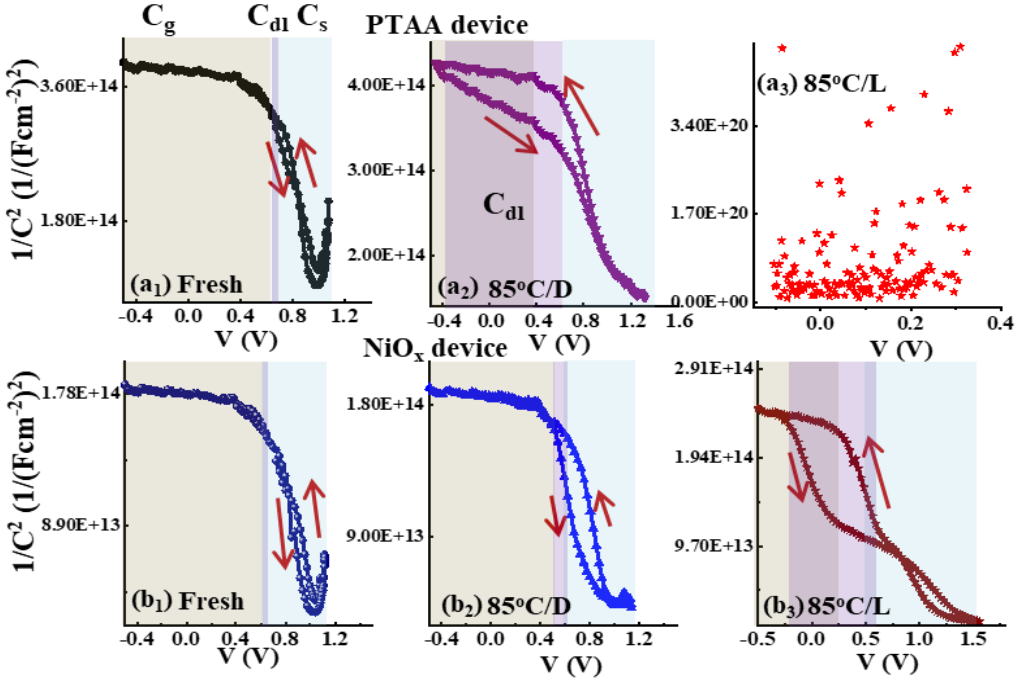

Figure 5. Mott–Schottky (*M–S*) plots (10 kHz) of PTAA and NiO_x devices under stress ageing: (a_1, b_1) fresh; (a_2, b_2) at 85 °C in dark; (a_3, b_3) at 85 °C under illumination for 1000 h. Shading indicates characteristic capacitance regime. Arrows indicate forward/reverse scan direction during *C–V* data collection. The double shaded regimes (a_2 and b_3) indicate the lagging of C-V curve by interfacial deterioration.

To unravel the deterioration of HaPSCs with ageing by optoelectronic means, we investigated the capacitance characteristics of aged devices. The capacitance response accounts for the carrier density (free carriers and defect density) distribution, [55,56] ion dynamics, [57,58] and charge accumulation at the interface [59,60] in the solar cell. Mott–Schottky (*M–S*) plots of devices aged under different conditions are presented in the Supporting Information (Figs. S25, S26). Representative *M–S* plots of PTAA and NiO_x devices are shown in Fig. 5 (fresh, 85 °C/dark, 85 °C/light). The *M–S* characteristics (Fig. 5a_1, b_1) of fresh devices reveal a voltage-independent fully depleted curve before the diffusion potential is

reached ($V_D \approx 0.96$ V), suggesting a wide intrinsic p–i–n junction that stems from geometrical capacitance (C_g).[61,62] A sharp transition of *M–S* curves indicates a negligible depletion layer capacitance (C_{dl}) regime that we attribute to low defect density. One can see a small capacitance (C_s) regime near the diffusion potential caused by charge accumulation at the interface and electrode polarization. A small hysteresis feature indicates lagging of ionic motion during the forward and reverse scan directions.[58,63] The characteristics of devices aged at 85 °C show many distinct features. The *M–S* curves of the PTAA device aged in the dark show deterioration of the intrinsic p–i–n junction and pronounced hysteresis, while that of the PTAA device aged under light shows no characteristics response, indicating a dead device. The *M–S* characteristics of aged PTAA devices show a voltage-dependent capacitance with increasing hysteresis (Fig. S25). These characteristics are pronounced in the device aged under heat and light. These results corroborate that the PTAA device degrades with the loss of intrinsic junction characteristics and increasing dominance of the lag of interfacial ionic motion with an increase in temperature, even in the dark. Rapid device degradation under light is associated with an accelerated deterioration of the intrinsic junction as a consequence of a wider C_{dl} regime and accumulation of higher ionic density at the interface.

Unlike in PTAA devices, the intrinsic p–i–n analogous to C_g is mostly retained in NiO_x devices aged under heat/dark (Fig. S26), with a slight change in the C_{dl} regime at different temperatures. This indicates that despite the adulteration of the interface by elemental diffusion or chemical interaction with ageing, the bulk layer is comparatively intact. On the other hand, in the NiO_x device aged under heat/light, although the *M–S* characteristics are not much different except for an increase in capacitance–voltage (*C–V*) hysteresis in the devices aged at ≤60 °C/light, one can see a pronounced change in M–S curves of the device aged at 85 °C/light. As depicted in Fig. 5b$_3$, although the NiO_x device (85 °C/light) shows a narrow intrinsic junction with a much wider range of C_{dl} coupled with significantly pronounced *C–V* hysteresis, it still has an intrinsic characteristic feature. These results corroborate that although the NiO_x device forms a comparatively stable interface and keeps the HaP layer intact even under harsh heat/dark/light conditions, ageing affects the optoelectronic quality of the interfacial layer. This makes it imperative to use a chemically inert, moisture-resistive CTL or additional protective layer to slow device degradation.

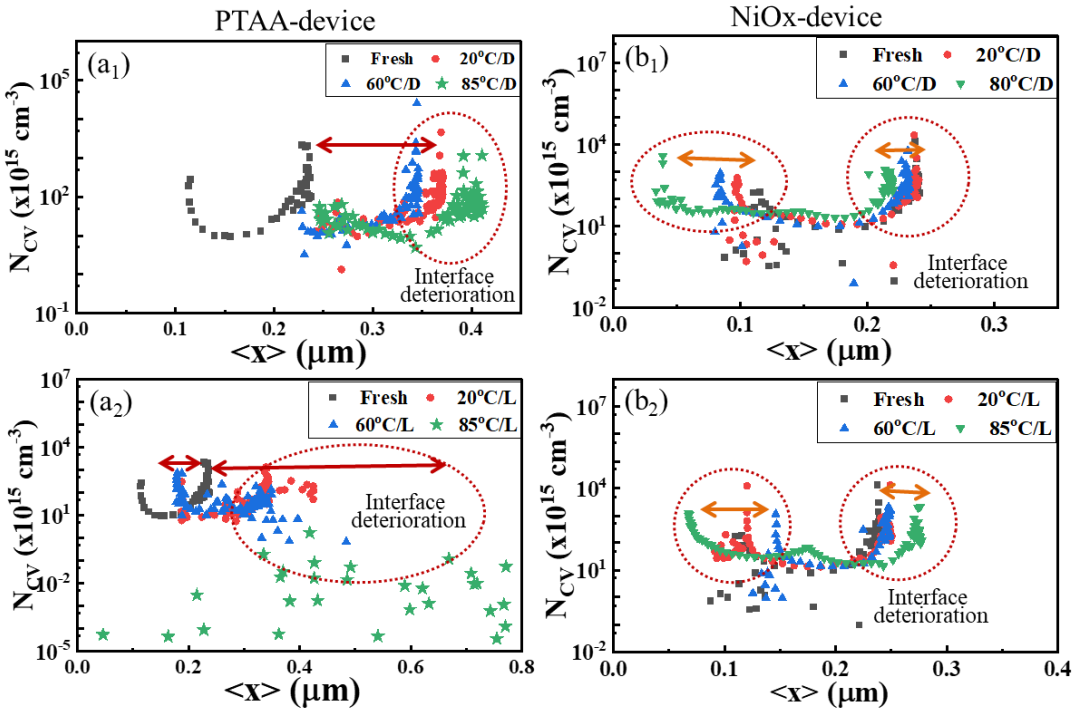

Figure 6. Carrier distribution profiles of aged devices under stress ageing: (a_1, a_2) PTAA and (b_1, b_2) NiO_x at 20, 60, and 85 °C under heat/dark or light treatment for 1000 h. The *C–V* carrier profiles are obtained from *C–V* curves at 10 kHz. Arrows indicate carrier profile shifting with reference to fresh device.

To get insight into the carrier profile, we analysed the *C–V* data to estimate the carrier distribution (N_{CV}) given by the relation,[64]

$$N_{CV} = -\frac{2}{q\varepsilon_0\varepsilon_s}\left[\frac{d}{dV}\left(\frac{1}{C^2}\right)\right]^{-1} \qquad (1)$$

where C is capacitance per area, ε_0 is permittivity of free space, ε_s is a dielectric constant of perovskite layer which is estimated from the plateau region of capacitance-frequency (*C-f*) plot measured at zero bias under dark as mentioned in our earlier reports.[33,65] Note that the *C–V* carrier distribution comprises the free charge carriers and defect density. The change in N_{CV} in the aged device is associated mainly with the defect profile in the bulk and interface. In PTAA, although there is no significant change in the *C–V* profile density (~9×10^{15} cm^{-3}) in the bulk, one can see an increase in carrier density (interface defect) of ~2–5 × 10^{18} cm^{-3} at the interface under ageing conditions (except 85 °C/light). The N_{CV} profiles (Fig. 6a_1) of the device under heat/dark are shifted ~80–120 nm with respect to the fresh device, and that of the aged devices are slightly wider at 60 °C/light and 20 °C/light with encroachment at both edges. The N_{CV} profile of the device at 85 °C/light resembles that of a non-functioning device. This behaviour is reproduced by the simulation described below (Fig. S29), indicating that the perovskite layer and its interface degraded with ageing. On the other hand, the N_{CV} profile of the aged NiO_x device (Fig. 6b_1, b_2) shows a *C–V* profile density of the bulk carrier of ~7.6 ×

10^{15} cm^{-3} and a carrier profile (interface defect) of ~1–3 × 10^{18} cm^{-3}, both in the range of the PTAA device, but the N_{CV} distribution was shifted only ~10–40 nm for device dark/light with reference to the fresh NiO_x device. A greater shift (~40 nm) is notable in the devices aged at 85 °C/dark/light, indicating a much lower interfacial deterioration than in PTAA devices aged under heat/dark. Thus, the *C–V* profile analysis corroborates that heat/light/dark ageing severely deteriorates the interface of the PTAA device, but does not increase the interface defect density. The more robust and inert interface of the NiO_x device restricts spurious elemental diffusion and complex interface chemistry.

To understand the degradation trend better, we simulated devices in SCAPS software (v. 3.3.07),[66] defining device configurations resembling real devices (Fig. S27). The layer properties were adopted from our earlier reports [65,67] and the optoelectronic properties were estimated from device analysis. The aged device characteristics were simulated by accounting for the effects on the bulk, interface quality, and CTL. The simulation results (Fig. S28a, b) show that the variation in the thickness of the interface defective layer (IDL) inferred from shifting of the N_{CV} profile (Fig. 6) with ageing drives the device degradation with a decrease in the J_{sc} and V_{oc}. Figure S28c relates the effect of the deterioration of CTL to degradation. It shows that if the CTL conductivity decreases with ageing, it significantly affects the *J–V* characteristics, resulting in a pronounced kink. In addition, the simulation results show that a defective HTL interface (HIF) with ageing might not be as detrimental as a defective HaP interface (i.e. IDL) (Fig. S28d) if the conductivity of HTL layer remains intact (Fig. S28c). Of course, device deterioration occurs jointly with bulk, interface, and CTL deterioration, depending on the layer properties. As we varied the CTL and interface deterioration, the simulation results (Fig. S28e) reveal a faster degradation of device parameters. These trends support the degradation characteristics of the PTAA devices, suggesting that degradation is governed by interface as well as bulk layer deterioration. Unlike PTAA, the aged NiO_x devices have no **S**-shaped *J–V* characteristics (Fig. S5). This implies that the NiO_x layer was not denatured under ageing, and conductivity is good enough to retain the *J–V* curve. These results suggest that the NiO_x device has a more robust interface, which mitigates the defect chemistry at the interface and in the bulk. Moreover, the simulation results of the N_{CV} profile (Fig. S29a, b) show that the IDL deterioration ($N_{t\text{-IDL}}$ and t_{IDL}) predominantly affects the carrier distribution in the device, supporting the carrier distribution in aged devices (Fig. 6). On the other hand, the defective layer induced in HIF does not affect the carrier profile much, so the carrier distribution in aged devices originates mainly from CTL/HaP interface deterioration. This implies that PTAA device degradation is dominated by PTAA/HaP deterioration following the denaturing of PTAA, whereas the NiO_x device develops a thin-layer IDL at the NiO_x/HaP interface and HIF without much loss of NiO_x properties. Thus, our simulation results partly explain the characteristics of degradation,

accounting for the deterioration of device layers and the interface. These results underline that the degradation of the HaPSCs is a collective consequence of a gradual worsening of both interface quality and HaP. The rate of degradation is also influenced by the nature of the CTL used.

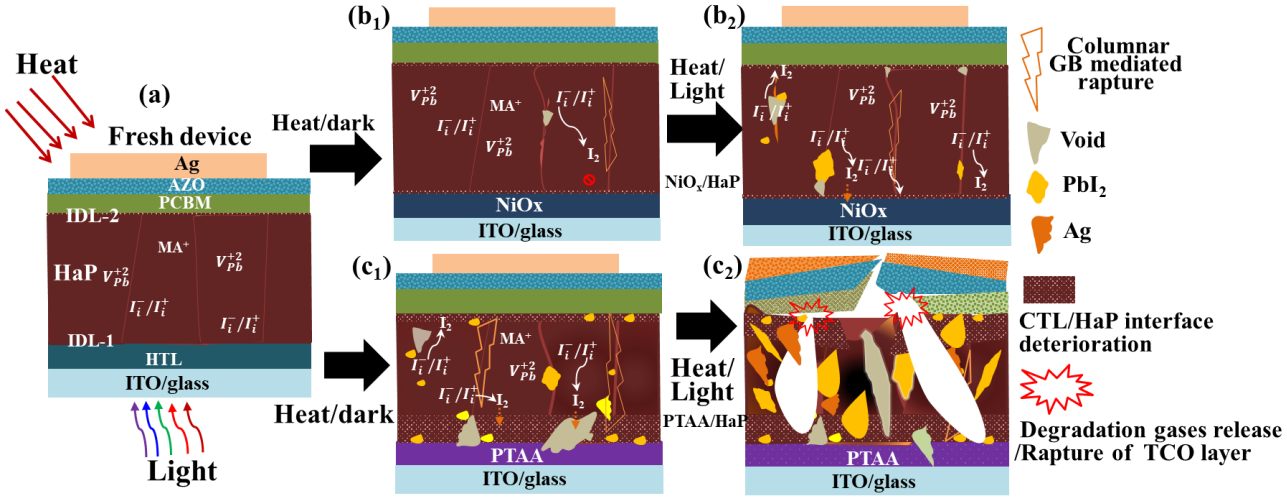

Figure 7. Schematic illustration of the degradation of PTAA and NiO_x devices under heat and light stress. (a) Fresh device structure. (b) NiO_x device aged under (b_1) heat/dark and (b_2) heat/light. (c) PTAA device aged under (c_1) heat/dark and (c_2) heat/light; top electrode ruptured. The white feature in (c_2) corresponds to hollow space or cracking.

Figure 7 illustrates the heat-driven degradation of the PTAA and NiO_x devices inferred from the above experimental results. We propose a columnar inter-grain degradation mechanism triggered by decomposition and mediated by both (HTL or ETL/HaP) interfaces deterioration to account for degradation in devices under heat/dark/light stress. Here, the normal point defect model was assumed to explain the device deterioration. Petrozza and co-workers [68] documented that the defect chemistry in HaP is dominated by interstitial halide (I_i) and lead/halogen vacancy (V_{Pb}/V_I) defect states. We assume a HaP bulk layer with defects and well-defined columnar grain (Fig. 7a). This structure suggests that defect dynamics is stimulated in the HaP bulk under illumination. As a result, the charge interstitial halogen defect (I_i^+/I_i^-) could react to form I_2 molecules following the trap filling reaction (Fig. 7b_1, c_1). [44] As the device is placed under heat and light, the defect sites in the HaP are activated (Fig. 7b_2, c_2). From the STEM results and XRD analysis, we speculate that the defect chemistry initially takes place at the intercolumnar grain boundaries. Importantly, the interaction of interstitial or vacancy defects of iodine leads to the formation of I_2 molecules that become trapped at the grain boundary. Then the I_2 gas diffuses to the neighbouring crystal grain through inter-grain boundaries and forms voids (Fig. 7b, c). Thus, the local decomposition of HaP is triggered by the loss of volatile MA^+ and the formation of I_2 and PbI_2. [18,19] Since the PTAA layer is more vulnerable to reaction with iodine and the ingress of moisture, the HaP bulk degradation is accelerated by the formation of PbI_2 at the

interface or inter-grain boundaries and the release of I_2 and other gases. [7] As the PTAA device is operated at high temperature under illumination for a longer time, the rate of HaP decomposition increases with the release of volatile by-products, which exert gaseous pressure in the bulk and interface. This induces a wider IDL. Hence, it corrodes the interfacial layer as well as the electrode through elemental diffusion; gradually weakens the interfacial junctions; and eventually ruptures the transparent conducting oxide and electrode layer by releasing the gaseous degradation product (Fig. $7c_2$).

On the other hand, despite the presence of inherent defects in the bulk layer, the NiO_x device remains intact under heat/dark ageing. Unlike in the PTAA device, the notorious defect chemistry in the bulk or at the interface is less severe under heat/dark ageing because the defect filling reactions are much slower owing to better stability and the robust NiO_x and its stable HaP/NiO_x interface (Fig. $7b_1$). Under illumination, the defect chemistry is activated at inter-columnar grains or in the off-stoichiometric bulk layer because of photo-excitation. This results in the formation of I_2 gas and PbI_2 crystallites under prolonged illumination. Since the NiO_x layer is poorly reactive to iodine and moisture which could ingress from the edge of the seal, the rate of formation of deleterious gaseous products is much suppressed. Therefore, the bulk degradation via internal defect dynamics and I_2 gas is significantly quenched (Fig. $7b_2$). Hence, it slows down the device deterioration relative to the PTAA device. However, we speculate that the mobile ionic defect ($I_i^-/I_i^0/I_i^-$) or I_2 gas formed by defect filling interacts slightly with hydroxy derivatives (such as, $Ni(OH)_2$, NiOOH, etc) in NiO_x film[69] at NiO_x/HaP interface to form a very thin NiI_2 interface layer with the release of water resulting in a slight deterioration of the HaP/NiO_x interface at higher temperatures under illumination. The chemical reaction for the formation of NiI_2 is illustrated by following reactions.

$$NiO_x + xNi(OH)_2 + x\ I^-/I^+ + h\vartheta \rightarrow NiO_x + xNiI_2 + xH_2O$$

$$NiO_x + xNiOOH + x\ I^-/I^+ + h\vartheta \rightarrow NiO_x + xNiI_2 + xH_2O$$

Heat and light driven the iodine related photochemical dynamics catalyzing perovskite degradation are given by chemical reaction.[19,44]

$$I^-/I^+ + 1e \rightleftarrows I^0/I^- + h\vartheta \rightleftarrows 2I_i^0 \rightleftarrows I_2 + h\vartheta$$

$$MAPbI_3 \rightleftarrows PbI_2 + MA^+ + I^-$$

This interlayer changes the interface potential profile and could decrease the photocurrent with a slight increase in V_{oc}, as observed in the experiment (Fig. $S5b_1$-b_3). Furthermore, it has been documented that the $MAPbI_3$ molecules partially decompose forming an intermediate complex ($[(MA^+)_{n-1}(CH_3NH_2)_n PbI_3][H_3O]$) with H_2O as a Lewis base.[45,70] It decomposes into HI(aq), CH_3NH_2(g), and PbI_2(s) only if

the HI has saturated the H_2O or the vapor pressure of CH_3NH_2 has reached equilibrium. We contemplate that the density of hydroxy derivatives in NiOx is not high (XPS spectra, Fig. S19) so that the H_2O by-product may not be large enough to saturated HI-H_2O or to achieve the vapor pressure of CH_3NH_2 high enough to decompose the intermediate hydrated perovskite complex. This might cause an intermediate complex of $MAPbI_3$ molecules stay at interface rather than completely decompose them which could be less deleterious for NiO_x/HaP interface. Although the NiO_x device is comparatively stable, it is important to passivate the interaction of mobile defects in the bulk layer to prevent the formation of iodine gas, which initiates the degradation of HaP and its interface.

Our results show that operational stability is influenced mainly by the contact layer. The degradation originates from the deterioration of the HaP bulk via inter-grains as a consequence of the formation of I_2 vapour by filling iodine-related defects, which triggers HaP decomposition and worsens the interface quality, as in previous studies. [7,18,20] Besides a robust and moisture-resistive CTL, inter-grain boundary and HaP/CTL interface passivation could be propitious for the improvement of the operational stability of HaPSCs.

4. Conclusions

This report presents insights into the operational stability of encapsulated HaPSCs at different temperatures for >1000 h under constant illumination in ambient air. We investigated the mechanism of degradation of devices made with PTAA or NiO_x as the HTL in dark and light at 20, 60, and 85 °C. Degradation of PTAA devices is accelerated by interface deterioration and bulk decomposition initiated by the formation of voids by the release of I_2 gas from defective regions at the columnar grain boundaries. The NiO_x devices had significantly better device stability because of their chemically inert and moisture-resistive properties. NiO_x formed a stable interface that suppresses I_2 gas formation and decelerates bulk decomposition by passivating the internal defect dynamics. Our results corroborate that the formation of voids with the release of I_2 gas and PbI_2 crystallites at the inter-grain or HTL/HaP interface is the primary cause of device degradation. Capacitance analysis suggests that the PTAA device develops a much wider interface defective layer than the NiO_x device, which leads to a decrease in J_{sc}. Deterioration of the HTL/HaP interface or widening of the interface defective layer is driven mainly by elemental diffusion and chemical reaction of I_2 gas with the interfacial layer. These results suggest that it is imperative to design device architecture to insert a moisture-resistive and chemically inert interfacial layer that can passivate the deterioration of the inter-grain of the HaP bulk and the HaP/CTL interface for the improvement of the operational stability of HaPSCs. Furthermore, we posit that this understanding for NiOx or PTAA as HTL in perovskite solar cells can be extended to other metal oxide systems (such as CuO_x, MoO_x, VO_x, etc.) and other polymer-based HTLs.

Experimental Methods

Device Fabrication:

The patterned indium tin oxide (ITO) coated glass substrates (15 Ω square^{-1}) were pre-cleaned in an ultrasonic bath with detergent, pure water, and 2-propanol, followed by an ultraviolet-ozone treatment for 5 min to remove the organic residuals. Firstly, we have prepared PTAA and NiOx on ITO glass. The details of PTAA (2 mg/ml in CB) film deposition have been mentioned in our earlier reports.[65,67] Nickel oxide (NiOx) was prepared by a sputtering method in supporting information. For the fabrication of perovskite films, the PbI_2 solution was prepared by dissolving PbI_2 (500 mg/ml) in a mixture of anhydrous DMF/DMSO (5:1 ratio) at 500 rpm/ 70^{o}C for 12 hours. The MAX (MAI and MACl) solution (50 mg ml^{-1}; 19:1 ratio) in ethanol at 300 rpm/ 50^{o}C for 12 hours. The PbI_2 precursor solution was spin-coated at 3000 rpm for 90 s and the MAX precursor solution (a mixture of MAI + MACl) was subsequently spun onto the PbI_2 layer at 4000 rpm, for 30 s. Those as grown $CH_3NH_3PbI_{3-x}Cl_x$ (x=0.002)perovskite films were simply placed on the hot plate with MACl powder covered with a petri dish at 100 ^{o}C to promote the crystallization.[65] For ETL deposition, PCBM (20 mg/ml in CB) was spin-coated on top of the films at 700 rpm for 30 s and 4000 rpm for 10 s and annealed at 100 ^{o}C for 15 min. Then a thin AZO layer (~25 nm) was deposited at 2500 rpm for 25 s and annealed at 100 ^{o}C for 10 min. To complete the device structure, samples were then transferred into the evaporation chamber connected to the glove box for metal contact deposition. Finally, 140 nm of Ag was thermally evaporated at a pressure <10^{-4} Pa. Devices with the area of 1 cm^2 were sealed by encapsulation glass and UV-curable resins (UV-RESIN XNR5516Z; Nagase ChemteX, Japan) before the subsequent measurement in ambient conditions.

ASSOCIATED CONTENT

Supporting Information

The Supporting Information is available free of charge on the ACS Publications website.

Experimental Method, Photograph of devices, experimental setting for device testing, Photos of aged devices, Table of aging conditions, J-V characteristics of aged devices, Device parameters trends, Absorption spectra, STEM cross-sectional images of aged devices and fresh device, STEM-EDX mapping/line profile, Experimental set up for thermal and illumination stress on perovskite films or

CTL films. XPS spectra of CTL under different treatment conditions, Tabulated data of XPS analysis, Capacitance-voltage curves of aged devices, Schematic of simulation, Simulation results of J-V, and carrier profile.

AUTHOR INFORMATION

Corresponding author.
*Email:KHADKA.B.Dhruba@nims.go.jp (D.B.K.)

ORCID

Dhruba B. Khadka: 0000-0001-9134-3890
Yasuhiro Shirai: 0000-0003-2164-5468
Masatoshi Yanagida: 0000-0002-8065-7875
Kenjiro Miyano: 0000-0002-5869-3087

Notes

The authors declare no competing financial interest.

Acknowledgements

This work was supported by Yazaki Memorial Foundation for Science and Technology.

References

(1) Kojima, A.; Teshima, K.; Shirai, Y.; Miyasaka, T. Organometal Halide Perovskites as Visible-Light Sensitizers for Photovoltaic. *J. Am. Chem. Soc.* **2009**, *131*, 6050–6051. https://doi.org/10.1021/ja809598r CCC:

(2) Brenner, T. M.; Egger, D. A.; Kronik, L.; Hodes, G.; Cahen, D. Hybrid Organic-Inorganic Perovskites: Low-Cost Semiconductors with Intriguing Charge-Transport Properties. *Nat. Rev. Mater.* **2016**, *1*, 15007. https://doi.org/10.1038/natrevmats.2015.7.

(3) Jeong, J.; Kim, M.; Seo, J.; Lu, H.; Ahlawat, P.; Mishra, A.; Yang, Y.; Hope, M. A.; Eickemeyer, F. T.; Kim, M.; Yoon, Y. J.; Choi, I. W.; Darwich, B. P.; Choi, S. J.; Jo, Y.; Lee, J. H.; Walker, B.; Zakeeruddin, S. M.; Emsley, L.; Rothlisberger, U.; Hagfeldt, A.; Kim, D. S.; Grätzel, M.; Kim, J. Y. Pseudo-Halide Anion Engineering for α-FAPbI3 Perovskite Solar Cells. *Nature* **2021**, *592* (7854), 381–385. https://doi.org/10.1038/s41586-021-03406-5.

(4) Saliba, M.; Stolterfoht, M.; Wolff, C. M.; Neher, D.; Abate, A. Measuring Aging Stability of Perovskite Solar Cells. *Joule* **2018**, *2* (6), 1019–1024. https://doi.org/10.1016/j.joule.2018.05.005.

(5) Rong, Y.; Hu, Y.; Mei, A.; Tan, H.; Saidaminov, M. I.; Seok, S. Il; McGehee, M. D.; Sargent, E. H.; Han, H. Challenges for Commercializing Perovskite Solar Cells. *Science* **2018**, *361* (6408), eaat8235. https://doi.org/10.1126/science.aat8235.

(6) Tress, W.; Domanski, K.; Carlsen, B.; Agarwalla, A.; Alharbi, E. A.; Graetzel, M.; Hagfeldt, A. Performance of Perovskite Solar Cells under Simulated Temperature-Illumination Real-World Operating Conditions. *Nat. Energy* **2019**, *4* (7), 568–574. https://doi.org/10.1038/s41560-019-0400-8.

(7) Han, Y.; Meyer, S.; Dkhissi, Y.; Weber, K.; Pringle, J. M.; Bach, U.; Spiccia, L.; Cheng, Y.-B. Degradation Observations of Encapsulated Planar CH3NH3PbI3 Perovskite Solar Cells at High Temperatures and Humidity. *J. Mater. Chem. A* **2015**, *3* (15), 8139–8147. https://doi.org/10.1039/C5TA00358J.

(8) Yang, J.; Siempelkamp, B. D.; Liu, D.; Kelly, T. L. Investigation of CH3NH3PbI3 Degradation Rates and Mechanisms in Controlled Humidity Environments Using in Situ Techniques. *ACS Nano* **2015**, *9* (2), 1955–1963. https://doi.org/10.1021/nn506864k.

(9) Zhao, J.; Deng, Y.; Wei, H.; Zheng, X.; Yu, Z.; Shao, Y.; Shield, J. E.; Huang, J. Strained Hybrid Perovskite Thin Films and Their Impact on the Intrinsic Stability of Perovskite Solar Cells. *Sci. Adv.* **2017**, *3* (11), eaao5616. https://doi.org/10.1126/sciadv.aao5616.

(10) Khenkin, M. V.; K. M., A.; Visoly-Fisher, I.; Kolusheva, S.; Galagan, Y.; Di Giacomo, F.; Vukovic, O.; Patil, B. R.; Sherafatipour, G.; Turkovic, V.; Rubahn, H.-G.; Madsen, M.; Mazanik, A. V.; Katz, E. A. Dynamics of Photoinduced Degradation of Perovskite Photovoltaics: From Reversible to Irreversible Processes. *ACS Appl. Energy Mater.* **2018**, *1* (2), 799–806. https://doi.org/10.1021/acsaem.7b00256.

(11) Schloemer, T. H.; Raiford, J. A.; Gehan, T. S.; Moot, T.; Nanayakkara, S.; Harvey, S. P.; Bramante, R. C.; Dunfield, S.; Louks, A. E.; Maughan, A. E.; Bliss, L.; McGehee, M. D.; van Hest, M. F. A. M.; Reese, M. O.; Bent, S. F.; Berry, J. J.; Luther, J. M.; Sellinger, A. The Molybdenum Oxide Interface Limits the High-Temperature Operational Stability of Unencapsulated Perovskite Solar Cells. *ACS Energy Lett.* **2020**, *5* (7), 2349–2360. https://doi.org/10.1021/acsenergylett.0c01023.

(12) Jena, A. K.; Ikegami, M.; Miyasaka, T. Severe Morphological Deformation of Spiro-OMeTAD in (CH 3 NH 3)PbI 3 Solar Cells at High Temperature. *ACS Energy Lett.* **2017**, *2* (8), 1760–1761. https://doi.org/10.1021/acsenergylett.7b00582.

(13) Planes, E.; Perrin, L.; Matheron, M.; Spalla, M.; Berson, S.; Flandin, L. Degradation Mechanisms in a Mixed Cations and Anions Perovskite Solar Cell: Mitigation Effect of the Gold Electrode. *ACS Appl. Energy Mater.* **2021**, *4* (2), 1365–1376. https://doi.org/10.1021/acsaem.0c02613.

(14) Bella, F.; Griffini, G.; Correa-Baena, J.-P.; Saracco, G.; Gratzel, M.; Hagfeldt, A.; Turri, S.; Gerbaldi, C. Improving Efficiency and Stability of Perovskite Solar Cells with Photocurable Fluoropolymers. *Science* **2016**, *354* (6309), 203–206. https://doi.org/10.1126/science.aah4046.

(15) Ma, S.; Bai, Y.; Wang, H.; Zai, H.; Wu, J.; Li, L.; Xiang, S.; Liu, N.; Liu, L.; Zhu, C.; Liu, G.; Niu, X.; Chen, H.; Zhou, H.; Li, Y.; Chen, Q. 1000 h Operational Lifetime Perovskite Solar Cells by Ambient Melting Encapsulation. *Adv. Energy Mater.* **2020**, *10* (9). https://doi.org/10.1002/aenm.201902472.

(16) Boyd, C. C.; Cheacharoen, R.; Leijtens, T.; McGehee, M. D. Understanding Degradation Mechanisms and Improving Stability of Perovskite Photovoltaics. *Chem. Rev.* **2019**, *119* (5), 3418–3451. https://doi.org/10.1021/acs.chemrev.8b00336.

(17) Conings, B.; Drijkoningen, J.; Gauquelin, N.; Babayigit, A.; D'Haen, J.; D'Olieslaeger, L.; Ethirajan, A.; Verbeeck, J.; Manca, J.; Mosconi, E.; Angelis, F. De; Boyen, H.-G. Intrinsic Thermal Instability of Methylammonium Lead Trihalide Perovskite. *Adv. Energy Mater.* **2015**, *5* (15), 1500477. https://doi.org/10.1002/aenm.201500477.

(18) Fu, F.; Pisoni, S.; Jeangros, Q.; Sastre-Pellicer, J.; Kawecki, M.; Paracchino, A.; Moser, T.; Werner, J.; Andres, C.; Duchêne, L.; Fiala, P.; Rawlence, M.; Nicolay, S.; Ballif, C.; Tiwari, A. N.; Buecheler, S. I 2 Vapor-Induced Degradation of Formamidinium Lead Iodide Based Perovskite Solar Cells under Heat–Light Soaking Conditions. *Energy Environ. Sci.* **2019**, *12* (10), 3074–3088. https://doi.org/10.1039/C9EE02043H.

(19) Wang, S.; Jiang, Y.; Juarez-Perez, E. J.; Ono, L. K.; Qi, Y. Accelerated Degradation of Methylammonium Lead Iodide Perovskites Induced by Exposure to Iodine Vapour. *Nat. Energy* **2017**, *2* (1), 16195. https://doi.org/10.1038/nenergy.2016.195.

(20) Wang, Q.; Chen, B.; Liu, Y.; Deng, Y.; Bai, Y.; Dong, Q.; Huang, J. Scaling Behavior of Moisture-Induced Grain Degradation in Polycrystalline Hybrid Perovskite Thin Films. *Energy Environ. Sci.* **2017**, *10* (2), 516–522. https://doi.org/10.1039/C6EE02941H.

(21) Ahn, N.; Kwak, K.; Jang, M. S.; Yoon, H.; Lee, B. Y.; Lee, J.; Pikhitsa, P. V; Byun, J.; Choi, M. Trapped Charge-Driven Degradation of Perovskite Solar Cells. *Nat. Commun.* **2016**, *7*, 13422. https://doi.org/10.1038/ncomms13422.

(22) Rolston, N.; Printz, A. D.; Tracy, J. M.; Weerasinghe, H. C.; Vak, D.; Haur, L. J.; Priyadarshi, A.; Mathews, N.; Slotcavage, D. J.; McGehee, M. D.; Kalan, R. E.; Zielinski, K.; Grimm, R.

L.; Tsai, H.; Nie, W.; Mohite, A. D.; Gholipour, S.; Saliba, M.; Grätzel, M.; Dauskardt, R. H. Effect of Cation Composition on the Mechanical Stability of Perovskite Solar Cells. *Adv. Energy Mater.* **2017**, 1702116. https://doi.org/10.1002/aenm.201702116.

(23) Liu, Y.; Akin, S.; Pan, L.; Uchida, R.; Arora, N.; Milić, J. V; Hinderhofer, A.; Schreiber, F.; Uhl, A. R.; Zakeeruddin, S. M.; Hagfeldt, A.; Dar, M. I.; Grätzel, M. Ultrahydrophobic 3D/2D Fluoroarene Bilayer-Based Water-Resistant Perovskite Solar Cells with Efficiencies Exceeding 22%. *Sci. Adv.* **2019**, *5* (6), eaaw2543. https://doi.org/10.1126/sciadv.aaw2543.

(24) Lin, Y.-H.; Sakai, N.; Da, P.; Wu, J.; Sansom, H. C.; Ramadan, A. J.; Mahesh, S.; Liu, J.; Oliver, R. D. J.; Lim, J.; Aspitarte, L.; Sharma, K.; Madhu, P. K.; Morales-Vilches, A. B.; Nayak, P. K.; Bai, S.; Gao, F.; Grovenor, C. R. M.; Johnston, M. B.; Labram, J. G.; Durrant, J. R.; Ball, J. M.; Wenger, B.; Stannowski, B.; Snaith, H. J. A Piperidinium Salt Stabilizes Efficient Metal-Halide Perovskite Solar Cells. *Science* **2020**, *369* (6499), 96–102. https://doi.org/10.1126/science.aba1628.

(25) Shin, S. S.; Yeom, E. J.; Yang, W. S.; Hur, S.; Kim, M. G.; Im, J.; Seo, J.; Noh, J. H.; Seok, S. Il. Colloidally Prepared La-Doped BaSnO3 Electrodes for Efficient, Photostable Perovskite Solar Cells. *Science* **2017**, *356* (6334), 167–171. https://doi.org/10.1126/science.aam6620.

(26) Christians, J. A.; Schulz, P.; Tinkham, J. S.; Schloemer, T. H.; Harvey, S. P.; Tremolet de Villers, B. J.; Sellinger, A.; Berry, J. J.; Luther, J. M. Tailored Interfaces of Unencapsulated Perovskite Solar Cells for >1,000 Hour Operational Stability. *Nat. Energy* **2018**, *3* (1), 68–74. https://doi.org/10.1038/s41560-017-0067-y.

(27) Schelhas, L. T.; Li, Z.; Christians, J. A.; Goyal, A.; Kairys, P.; Harvey, S. P.; Kim, D. H.; Stone, K. H.; Luther, J. M.; Zhu, K.; Stevanovic, V.; Berry, J. J. Insights into Operational Stability and Processing of Halide Perovskite Active Layers. *Energy Environ. Sci.* **2019**, *12* (4), 1341–1348. https://doi.org/10.1039/C8EE03051K.

(28) Arora, N.; Dar, M. I.; Hinderhofer, A.; Pellet, N.; Schreiber, F.; Zakeeruddin, S. M.; Grätzel, M. Perovskite Solar Cells with CuSCN Hole Extraction Layers Yield Stabilized Efficiencies Greater than 20%. *Science* **2017**, *358* (6364), 768–771. https://doi.org/10.1126/science.aam5655.

(29) Yang, S.; Chen, S.; Mosconi, E.; Fang, Y.; Xiao, X.; Wang, C.; Zhou, Y.; Yu, Z.; Zhao, J.; Gao, Y.; De Angelis, F.; Huang, J. Stabilizing Halide Perovskite Surfaces for Solar Cell Operation with Wide-Bandgap Lead Oxysalts. *Science* **2019**, *365* (6452), 473 LP – 478. https://doi.org/10.1126/science.aax3294.

(30) Yang, N.; Zhu, C.; Chen, Y.; Zai, H.; Wang, C.; Wang, X.; Wang, H.; Ma, S.; Gao, Z.; Wang, X.; Hong, J.; Bai, Y.; Zhou, H.; Cui, B.-B.; Chen, Q. An in Situ Cross-Linked 1D/3D

Perovskite Heterostructure Improves the Stability of Hybrid Perovskite Solar Cells for over 3000 h Operation. *Energy Environ. Sci.* **2020**, *13* (11), 4344–4352. https://doi.org/10.1039/D0EE01736A.

(31) Akbulatov, A. F.; Frolova, L. A.; Dremova, N. N.; Zhidkov, I.; Martynenko, V. M.; Tsarev, S. A.; Luchkin, S. Y.; Kurmaev, E. Z.; Aldoshin, S. M.; Stevenson, K. J.; Troshin, P. A. Light or Heat: What Is Killing Lead Halide Perovskites under Solar Cell Operation Conditions? *J. Phys. Chem. Lett.* **2020**, *11* (1), 333–339. https://doi.org/10.1021/acs.jpclett.9b03308.

(32) Li, G.; Jiang, Y.; Deng, S.; Tam, A.; Xu, P.; Wong, M.; Kwok, H.-S. Overcoming the Limitations of Sputtered Nickel Oxide for High-Efficiency and Large-Area Perovskite Solar Cells. *Adv. Sci.* **2017**, *4* (12), 1700463. https://doi.org/10.1002/advs.201700463.

(33) Khadka, D. B.; Shirai, Y.; Yanagida, M.; Miyano, K. Unraveling the Impacts Induced by Organic and Inorganic Hole Transport Layers in Inverted Halide Perovskite Solar Cells. *ACS Appl. Mater. Interfaces* **2019**, *11* (7), 7055–7065. https://doi.org/10.1021/acsami.8b20924.

(34) Petrović, M.; Maksudov, T.; Panagiotopoulos, A.; Serpetzoglou, E.; Konidakis, I.; Stylianakis, M. M.; Stratakis, E.; Kymakis, E. Limitations of a Polymer-Based Hole Transporting Layer for Application in Planar Inverted Perovskite Solar Cells. *Nanoscale Adv.* **2019**, *1* (8), 3107–3118. https://doi.org/10.1039/c9na00246d.

(35) Thampy, S.; Zhang, B.; Hong, K. H.; Cho, K.; Hsu, J. W. P. Altered Stability and Degradation Pathway of CH3NH3PbI3 in Contact with Metal Oxide. *ACS Energy Lett.* **2020**, *5* (4), 1147–1152. https://doi.org/10.1021/acsenergylett.0c00041.

(36) Chaudhary, B.; Koh, T. M.; Febriansyah, B.; Bruno, A.; Mathews, N.; Mhaisalkar, S. G.; Soci, C. Mixed-Dimensional Naphthylmethylammonium-Methylammonium Lead Iodide Perovskites with Improved Thermal Stability. *Sci. Rep.* **2020**, *10* (1), 429. https://doi.org/10.1038/s41598-019-57015-4.

(37) Bonadio, A.; Escanhoela, C. A.; Sabino, F. P.; Sombrio, G.; de Paula, V. G.; Ferreira, F. F.; Janotti, A.; Dalpian, G. M.; Souza, J. A. Entropy-Driven Stabilization of the Cubic Phase of MaPbI3 at Room Temperature. *J. Mater. Chem. A* **2021**, *9* (2), 1089–1099. https://doi.org/10.1039/D0TA10492B.

(38) Whitfield, P. S.; Herron, N.; Guise, W. E.; Page, K.; Cheng, Y. Q.; Milas, I.; Crawford, M. K. Structures, Phase Transitions and Tricritical Behavior of the Hybrid Perovskite Methyl Ammonium Lead Iodide. *Sci. Rep.* **2016**, *6* (1), 35685. https://doi.org/10.1038/srep35685.

(39) Wang, Q.; Lyu, M.; Zhang, M.; Yun, J.-H.; Chen, H.; Wang, L. Transition from the Tetragonal to Cubic Phase of Organohalide Perovskite: The Role of Chlorine in Crystal Formation of CH 3 NH 3 PbI 3 on TiO 2 Substrates. *J. Phys. Chem. Lett.* **2015**, *6* (21), 4379–

4384. https://doi.org/10.1021/acs.jpclett.5b01682.

(40) Kim, T. W.; Uchida, S.; Matsushita, T.; Cojocaru, L.; Jono, R.; Kimura, K.; Matsubara, D.; Shirai, M.; Ito, K.; Matsumoto, H.; Kondo, T.; Segawa, H. Self-Organized Superlattice and Phase Coexistence inside Thin Film Organometal Halide Perovskite. *Advanced Materials*. February 1, 2018, p 1705230. https://doi.org/10.1002/adma.201705230.

(41) Kato, Y.; Ono, L. K.; Lee, M. V.; Wang, S.; Raga, S. R.; Qi, Y. Silver Iodide Formation in Methyl Ammonium Lead Iodide Perovskite Solar Cells with Silver Top Electrodes. *Adv. Mater. Interfaces* **2015**, *2* (13), 1500195. https://doi.org/10.1002/admi.201500195.

(42) Kulkarni, A.; Ünlü, F.; Pant, N.; Kaur, J.; Bohr, C.; Jena, A. K.; Öz, S.; Yanagida, M.; Shirai, Y.; Ikegami, M.; Miyano, K.; Tachibana, Y.; Chakraborty, S.; Mathur, S.; Miyasaka, T. Concerted Ion Migration and Diffusion-Induced Degradation in Lead-Free Ag 3 BiI 6 Rudorffite Solar Cells under Ambient Conditions. *Sol. RRL* **2021**, *5* (8), 2100077. https://doi.org/10.1002/solr.202100077.

(43) Boyd, C. C.; Cheacharoen, R.; Bush, K. A.; Prasanna, R.; Leijtens, T.; McGehee, M. D. Barrier Design to Prevent Metal-Induced Degradation and Improve Thermal Stability in Perovskite Solar Cells. *ACS Energy Lett.* **2018**, *3* (7). https://doi.org/10.1021/acsenergylett.8b00926.

(44) Motti, S. G.; Meggiolaro, D.; Barker, A. J.; Mosconi, E.; Perini, C. A. R.; Ball, J. M.; Gandini, M.; Kim, M.; De Angelis, F.; Petrozza, A. Controlling Competing Photochemical Reactions Stabilizes Perovskite Solar Cells. *Nat. Photonics* **2019**, *13* (8), 532–539. https://doi.org/10.1038/s41566-019-0435-1.

(45) Wang, Z.; Shi, Z.; Li, T.; Chen, Y.; Huang, W. Stability of Perovskite Solar Cells: A Prospective on the Substitution of the A Cation and X Anion. *Angewandte Chemie - International Edition*. 2017, pp 1190–1212. https://doi.org/10.1002/anie.201603694.

(46) Juarez-Perez, E. J.; Ono, L. K.; Maeda, M.; Jiang, Y.; Hawash, Z.; Qi, Y. Photodecomposition and Thermal Decomposition in Methylammonium Halide Lead Perovskites and Inferred Design Principles to Increase Photovoltaic Device Stability. *J. Mater. Chem. A* **2018**, *6* (20), 9604–9612. https://doi.org/10.1039/c8ta03501f.

(47) Juarez-Perez, E. J.; Hawash, Z.; Raga, S. R.; Ono, L. K.; Qi, Y. Thermal Degradation of CH3NH3PbI3 Perovskite into NH3 and CH3I Gases Observed by Coupled Thermogravimetry-Mass Spectrometry Analysis. *Energy Environ. Sci.* **2016**, *9* (11), 3406–3410. https://doi.org/10.1039/c6ee02016j.

(48) Biesinger, M. C.; Lau, L. W. M.; Gerson, A. R.; Smart, R. S. C. The Role of the Auger Parameter in XPS Studies of Nickel Metal, Halides and Oxides. *Phys. Chem. Chem. Phys.*

2012, *14* (7), 2434–2442. https://doi.org/10.1039/C2CP22419D.

(49) Zhang, B.; Su, J.; Guo, X.; Zhou, L.; Lin, Z.; Feng, L.; Zhang, J.; Chang, J.; Hao, Y. NiO/Perovskite Heterojunction Contact Engineering for Highly Efficient and Stable Perovskite Solar Cells. *Adv. Sci.* **2020**, *7* (11), 1903044. https://doi.org/10.1002/advs.201903044.

(50) Liu, X.; Cheng, Y.; Liu, C.; Zhang, T.; Zhang, N.; Zhang, S.; Chen, J.; Xu, Q.; Ouyang, J.; Gong, H. 20.7% Highly Reproducible Inverted Planar Perovskite Solar Cells with Enhanced Fill Factor and Eliminated Hysteresis. *Energy Environ. Sci.* **2019**, *12* (5), 1622–1633. https://doi.org/10.1039/C9EE00872A.

(51) Sun, X.; Ji, L. Y.; Chen, W. W.; Guo, X.; Wang, H. H.; Lei, M.; Wang, Q.; Li, Y. F. Halide Anion-Fullerene π Noncovalent Interactions: N-Doping and a Halide Anion Migration Mechanism in p-i-n Perovskite Solar Cells. *J. Mater. Chem. A* **2017**, *5* (39), 20720–20728. https://doi.org/10.1039/c7ta06335k.

(52) Moulder, J. F.; Stickle, W. F.; E.'Sobol, P.; Bomben, K. D. *Handbook of X-Ray Photoelectron Spectroscopy*; Chastain, J., Ed.; Perkin-Elmer Corporation, 1992.

(53) Dunlap-Shohl, W. A.; Li, T.; Mitzi, D. B. Interfacial Effects during Rapid Lamination within MAPbI3 Thin Films and Solar Cells. *ACS Appl. Energy Mater.* **2019**, *2* (7), 5083–5093. https://doi.org/10.1021/acsaem.9b00747.

(54) Boldyreva, A. G.; Zhidkov, I. S.; Tsarev, S.; Akbulatov, A. F.; Tepliakova, M. M.; Fedotov, Y. S.; Bredikhin, S. I.; Postnova, E. Y.; Luchkin, S. Y.; Kurmaev, E. Z.; Stevenson, K. J.; Troshin, P. A. Unraveling the Impact of Hole Transport Materials on Photostability of Perovskite Films and P-i-n Solar Cells. *ACS Appl. Mater. Interfaces* **2020**, *12* (16), 19161–19173. https://doi.org/10.1021/acsami.0c01027.

(55) Ni, Z.; Bao, C.; Liu, Y.; Jiang, Q.; Wu, W.-Q.; Chen, S.; Dai, X.; Chen, B.; Hartweg, B.; Yu, Z.; Holman, Z.; Huang, J. Resolving Spatial and Energetic Distributions of Trap States in Metal Halide Perovskite Solar Cells. *Science* **2020**, *367* (6484), 1352–1358. https://doi.org/10.1126/science.aba0893.

(56) Khadka, D. B.; Shirai, Y.; Yanagida, M.; Miyano, K. Degradation of Encapsulated Perovskite Solar Cells Driven by Deep Trap States and Interfacial Deterioration. *J. Mater. Chem. C* **2017**, *6* (1), 162–170. https://doi.org/10.1039/c7tc03733c.

(57) García-Rosell, M.; Bou, A.; Jiménez-Tejada, J. A.; Bisquert, J.; Lopez-Varo, P. Analysis of the Influence of Selective Contact Heterojunctions on the Performance of Perovskite Solar Cells. *J. Phys. Chem. C* **2018**, *122* (25), 13920–13925. https://doi.org/10.1021/acs.jpcc.8b01070.

(58) Miyano, K.; Yanagida, M.; Shirai, Y. Impedance Spectroscopy Revisited. *Adv. Energy Mater.* **2020**, *10* (26), 1903097. https://doi.org/10.1002/aenm.201903097.

(59) Moia, D.; Gelmetti, I.; Calado, P.; Fisher, W.; Stringer, M.; Game, O.; Hu, Y.; Docampo, P.; Lidzey, D.; Palomares, E.; Nelson, J.; Barnes, P. R. F. Ionic-to-Electronic Current Amplification in Hybrid Perovskite Solar Cells: Ionically Gated Transistor-Interface Circuit Model Explains Hysteresis and Impedance of Mixed Conducting Devices. *Energy Environ. Sci.* **2019**, *12* (4), 1296–1308. https://doi.org/10.1039/C8EE02362J.

(60) Kim, H.-S.; Jang, I.-H.; Ahn, N.; Choi, M.; Guerrero, A.; Bisquert, J.; Park, N.-G. Control of I – V Hysteresis in CH 3 NH 3 PbI 3 Perovskite Solar Cell. *J. Phys. Chem. Lett.* **2015**, *6* (22), 4633–4639. https://doi.org/10.1021/acs.jpclett.5b02273.

(61) Tsai, H.; Nie, W.; Blancon, J.-C.; Stoumpos, C. C.; Asadpour, R.; Harutyunyan, B.; Neukirch, A. J.; Verduzco, R.; Crochet, J. J.; Tretiak, S.; Pedesseau, L.; Even, J.; Alam, M. A.; Gupta, G.; Lou, J.; Ajayan, P. M.; Bedzyk, M. J.; Kanatzidis, M. G.; Mohite, A. D. High-Efficiency Two-Dimensional Ruddlesden–Popper Perovskite Solar Cells. *Nature* **2016**, *536* (7616), 312–316. https://doi.org/10.1038/nature18306.

(62) Zhang, X.; Zhang, J.; Phuyal, D.; Du, J.; Tian, L.; Öberg, V. A.; Johansson, M. B.; Cappel, U. B.; Karis, O.; Liu, J.; Rensmo, H.; Boschloo, G.; Johansson, E. M. J. Inorganic CsPbI 3 Perovskite Coating on PbS Quantum Dot for Highly Efficient and Stable Infrared Light Converting Solar Cells. *Adv. Energy Mater.* **2018**, *8* (6), 1702049. https://doi.org/10.1002/aenm.201702049.

(63) Chen, B.; Yang, M.; Priya, S.; Zhu, K. Origin of J-V Hysteresis in Perovskite Solar Cells. *J. Phys. Chem. Lett.* **2016**, *7* (5), 905–917. https://doi.org/10.1021/acs.jpclett.6b00215.

(64) Heath, J.; Zabierowski, P. Capacitance Spectroscopy of Thin-Film Solar Cells. In *Advanced Characterization Techniques for Thin Film Solar Cells: Second Edition*; 2016; Vol. 1–2, pp 93–119. https://doi.org/10.1002/9783527699025.ch4.

(65) Khadka, D. B.; Shirai, Y.; Yanagida, M.; Masuda, T.; Miyano, K. Enhancement in Efficiency and Optoelectronic Quality of Perovskite Thin Films Annealed in MACl Vapor. *Sustain. Energy Fuels* **2017**, *1* (4), 755–766. https://doi.org/10.1039/C7SE00033B.

(66) Burgelman, M.; Nollet, P.; Degrave, S. Modelling Polycrystalline Semiconductor Solar Cells. *Thin Solid Films* **2000**, *361*, 527–532. https://doi.org/10.1016/S0040-6090(99)00825-1.

(67) Khadka, D. B.; Shirai, Y.; Yanagida, M.; Ryan, J. W.; Miyano, K. Exploring the Effects of Interfacial Carrier Transport Layers on Device Performance and Optoelectronic Properties of Planar Perovskite Solar Cells. *J. Mater. Chem. C* **2017**, *5* (34), 8819–8827. https://doi.org/10.1039/C7TC02822A.

(68) Ball, J. M.; Petrozza, A. Defects in Perovskite-Halides and Their Effects in Solar Cells. *Nat. Energy* **2016**, *1* (11), 16149. https://doi.org/10.1038/nenergy.2016.149.

(69) Boyd, C. C.; Shallcross, R. C.; Moot, T.; Kerner, R.; Bertoluzzi, L.; Onno, A.; Kavadiya, S.; Chosy, C.; Wolf, E. J.; Werner, J.; Raiford, J. A.; de Paula, C.; Palmstrom, A. F.; Yu, Z. J.; Berry, J. J.; Bent, S. F.; Holman, Z. C.; Luther, J. M.; Ratcliff, E. L.; Armstrong, N. R.; McGehee, M. D. Overcoming Redox Reactions at Perovskite-Nickel Oxide Interfaces to Boost Voltages in Perovskite Solar Cells. *Joule* **2020**, *4* (8), 1759–1775. https://doi.org/10.1016/j.joule.2020.06.004.

(70) Frost, J. M.; Butler, K. T.; Brivio, F.; Hendon, C. H.; Van Schilfgaarde, M.; Walsh, A. Atomistic Origins of High-Performance in Hybrid Halide Perovskite Solar Cells. *Nano Lett.* **2014**, *14* (5), 2584–2590. https://doi.org/10.1021/nl500390f.

Table of Contents Graphics

The degradation of HaPSCs is initiated by the deterioration of the HaP bulk via inter-grains as a consequence of the formation of voids and PbI_2 crystallites at columnar inter-grains or the HTL(ETL)/HaP interfaces with the release of I_2 gas, which worsens interface quality. The rate of degradation is also influenced by the properties of CTL and the CTL/HaP interface quality.